Full length article

Additive manufacturing of hierarchical injectable scaffolds for tissue engineering

A. Béduer [a,b], N. Piacentini [b], L. Aeberli [b], A. Da Silva [c], C.A. Verheyen [b], F. Bonini [a], A. Rochat [d], A. Filippova [a], L. Serex [b], P. Renaud [b], T. Braschler [a,*]

[a] Department of Pathology and Immunology, Faculty of Medicine, University of Geneva, CMU, Rue Michel-Servet 1, 1211 Genève 4, Switzerland
[b] Laboratory of Microsystems 4, STI-IMT, Station 17, EPFL, 1015 Lausanne, Switzerland
[c] Center for Biomedical Imaging CIBM, ENT-R, Station 6, EPFL, 1015 Lausanne, Switzerland
[d] Department of Experimental Surgery, Pavillon 4, Lausanne University Hospital (CHUV), 1011 Lausanne, Switzerland

ARTICLE INFO

ABSTRACT

We present a 3D-printing technology allowing free-form fabrication of centimetre-scale injectable structures for minimally invasive delivery. They result from the combination of 3D printing onto a cryogenic substrate and optimisation of carboxymethylcellulose-based cryogel inks. The resulting highly porous and elastic cryogels are biocompatible, and allow for protection of cell viability during compression for injection. Implanted into the murine subcutaneous space, they are colonized with a loose fibrovascular tissue with minimal signs of inflammation and remain encapsulation-free at three months. Finally, we vary local pore size through control of the substrate temperature during cryogenic printing. This enables control over local cell seeding density *in vitro* and over vascularization density in cell-free scaffolds *in vivo*. In sum, we address the need for 3D-bioprinting of large, yet injectable and highly biocompatible scaffolds and show modulation of the local response through control over local pore size.

Statement of Significance

This work combines the power of 3D additive manufacturing with clinically advantageous minimally invasive delivery. We obtain porous, highly compressible and mechanically rugged structures by optimizing a cryogenic 3D printing process. Only a basic commercial 3D printer and elementary control over reaction rate and freezing are required. The porous hydrogels obtained are capable of withstanding delivery through capillaries up to 50 times smaller than their largest linear dimension, an as yet unprecedented compression ratio. Cells seeded onto the hydrogels are protected during compression. The hydrogel structures further exhibit excellent biocompatibility 3 months after subcutaneous injection into mice.

We finally demonstrate that local modulation of pore size grants control over vascularization density *in vivo*. This provides proof-of-principle that meaningful biological information can be encoded during the 3D printing process, deploying its effect after minimally invasive implantation.

1. Introduction

3D bioprinting [1] is an emerging, rapidly-evolving field with the potential to reproduce an ever-increasing list of human and animal tissues such as skin [2], neural tissue [3], intestine [4], liver [5] and even functional ovaries [6]. With precise spatial control in three dimensions, bioprinting offers freeform fabrication of highly sophisticated structures for tissue engineering. Unfortunately, the bulky and fragile nature of these 3D-printed scaffolds presents a major barrier to successful *in vivo* implantation. It is well-established that minimally invasive surgery significantly decreases surgical complications like inflammation [7], infection [8], adhesions [9,10] and scarring [11]. Current 3D-printed hydrogel scaffolds cannot be delivered in this manner, and development of large injectable 3D-printed scaffolds remains a major challenge in terms of the clinical relevance of the bioprinting field [12,13].

Numerous hydrogel strategies exist for minimally invasive implantation. *In situ* liquid gelation [14], fragmentation [15,16], geometric folding of 2D patches [13,17], and compression of highly porous and elastic cryogels [18–20] have all shown promise for minimally invasive cell and tissue delivery applications. However, these systems cannot offer the freeform fabrication and structuration provided by 3D printing techniques [12]. As such, tissue engineering currently lacks a technology that combines complex, yet facile 3D structuration with minimally invasive deployment *in vivo*. 4D bioprinting is a novel concept whereby 3D-printed structures gain time-evolving functionality [21] such as volume change [22] or shape-morphing capacity [21,23,24]. We propose that 4D printed [21,23,24] cryogels [18–20] could address the need for free-form fabrication for minimally invasive delivery.

The first objective of this study is the development of 3D printed structures that can be implanted *in vivo* in a minimally invasive fashion. For this, we exploit a 4D compressional shape change of 3D printed cryogel structures. We have recently developed a 3D cryogel printing process [25]. This technique allows the production of arbitrarily shaped cryogels with highly controlled local properties. Here, we adapt the process to obtain the required compressibility and mechanical ruggedness for minimally invasive delivery. Cryogels are synthesized from a liquid precursor in the frozen state, where ice crystals provide the template for gel pore structure [18]. Slow crosslinking after ice crystal formation then creates the exceptional elasticity required for minimally invasive delivery [20]. In 3D printing of structures suitable for minimally invasive delivery, strong adhesion between subsequently printed layers [26] is a particular challenge. Further, for *in vivo* implantation, the pore size needs to be adapted to obtain colonization and vascularization [27,28]. Suitably 3D-printed cryogel scaffolds can be dehydrated, which leads to spontaneous folding and compression. Due to their shape memory [18–20], the scaffolds can uptake fluid and resume their original shape and volume after rehydration [21,23,24]. This dehydration-rehydration cycle provides the scaffold with 4th dimensional, time-dependent functionality. We utilize the 4D deployment cycle for minimally invasive delivery of 3D-printed scaffolds *in vivo*.

Cryogel scaffolds have been shown to be suitable vehicles for minimally invasive delivery of adherent cells by offering protection from excessive compression forces during injection [19,20,29]. We here investigate the capacity of 3D-printed structures, which include designed local pore size variations [25], to provide cell protection during syringe injection.

Furthermore, scaffold biocompatibility is necessary for successful long-term implantation. We have previously shown *in vitro* biocompatibility of 3D printed cryogel structures [25]. *In vivo*, careful selection of raw materials [30] is required to prevent chronic inflammation and ensuing scaffold encapsulation [31–33]. We utilize carboxymethylcellulose as the structural material with adipic dihydrazide crosslinking chemistry, both known for their biocompatibility [34,35]. It is a further aim of this report to assess biocompatibility of the printed structures *in vivo*.

A final objective of this report is to provide proof of principle that designed and printed locally varying properties in 3D printed scaffolds for minimally invasive delivery can be used to drive the tissue response *in vivo*. Scaffolds can influence tissue in multiple ways, for instance through delivery of growth factors [29,36], small molecules [37], nucleic acid vectors [38], and cells [29], or through scaffold geometry itself [6,27,28]. Notably, efficient vascularization of porous, biocompatible scaffolds is closely linked to pore size [27,28]. Because cryogel pore structure depends on the freezing process [18,25], we use modulation of printing substrate temperatures to print cryogel deposits with locally varying pore structures. We then assess the capacity of the scaffolds to transfer the information contained in the 3D pore size pattern to cells and tissue.

We do so by quantifying local cell seeding density *in vitro*, and local tissue infiltration and local vascularization densities *in vivo*, at 3 months after minimally invasive delivery.

2. Materials and methods

2.1. Chemicals

Sodium carboxymethylcellulose CMC (419338-100G, 700 kDa), 2-(N-morpholino)ethanesulfonic acid MES (M3671-50G), N-(3-dimethylaminopropyl)-N′-ethylcarbodiimide hydrochloride EDC (E7750-25G), adipic acid dihydrazide (A0638-25G), NaOH (S8045-500G), aminofluorescein (07980 Fluka-1G), ethylene-diamine-tetraacetic acid EDTA (EDS), phosphate buffered saline PBS (P4417-50TAB), paraformaldehyde(158127-500 g), Triton X-100 (X100-100 mL), collagen I (C4243-20 mL), phalloidin-ATTO 565 (94072), aminoethanol (398136-500 mL), 4-(2-Hydroxyethyl) piperazine-1-ethanesulfonic acid HEPES (H3375), sodium carbonate Na_2CO_3 (S7795), HEPES buffered saline HBS (51558), and rhodamine B isothiocyanate (283924-100MG) were obtained from Sigma-Aldrich. Foetal bovine serum was from PAA Laboratories, and DMEM cell culture medium from GIBCO.

2.2. Cryogel reaction mix

Cryogels were synthesized using established cryogel chemistry [19], with modifications to allow for sufficient handling time during 3D printing (electronic Supplementary information 1). Briefly, carboxymethylcellulose was dissolved in 44 mM HEPES, pH 7.4, followed by addition of the crosslinker adipic acid dihydrazide (AAD) and activation by the carbodiimide EDC. The final reaction mixture contained 9 mg/mL carboxymethylcellulose, 0.3 mg/mL adipic dihydrazide, 44 mM HEPES pH 7.4, and was activated with 3.6 mg/mL EDC.

2.3. 3D printing

After activation with EDC, the reaction mixture was dispensed by a modified commercial 3D printer (Protos v2, SwissRepRap, Tardo GmbH, Subingen, Switzerland). For this the reaction mixture was placed in a pneumatically pressurized reservoir (ca. 600 mbar), which was connected via HPLC tubing to an electrovalve (the Lee Company, INKX0508000A, with nozzle INZA3330997D) mounted on the printing platform. We modified the printer firmware (open source) such as to output a constant opening signal to the valves during printing rather than the pulsed stepper motor on/off signal required for the extrusion, and used an amplification board as specified by the electrovalve manufacturer to drive the valves (the Lee Company, drawing LFIX1001750A). The Protos v2 printer is driven by G-Code through the Simplify3D software interface provided with the printer. For testing and simple structures, we typically provide the G-Code directly in the Simplify3D interface. For more complex structures, we generate the G-Code by slicing standard STL design files in the Simplify3D software. We fabricated the scaffolds by printing onto a stage held at sub-zero temperatures (−80 °C or −20 °C depending on the placement of the dry ice relative to the printing area, as measured in calibration experiments by a surface contact thermometer). We used a print rate of 2 mm/s, and a fluid flow rate of 300 μl/min (during opening of the electrovalve). This combination represents an optimal combination of printing quality and adequately large pore size (electronic Supplementary information 2). To control heat transfer, and simultaneously to enable facile sample transfer, we 3D print the gels on a polypropylene substrate (0.5 mm height), attached with a drop of isopropanol to the cooled printer stage.

After printing, the gels were placed in a −20 °C freezer. After 1 week, the cryogels were thawed, rinsed in DI, EDTA 10 mM and then PBS, and autoclave-sterilized in PBS. Green fluorescent cryogels were obtained by addition of aminofluorescein (final concentration 10 μM) during the crosslinking reaction (for details, see [19]). Red fluorescent cryogels were obtained by pre-reacting the adipic dihydrazide with rhodamine B isothiocyanate (final theoretical concentration 10 μM), leading to addition of the fluorescent label onto a small fraction of the adipic dihydrazide molecules.

2.4. Scaffold characterization

2.4.1. Scanning electron microscopy
For SEM imaging, cryogel samples are washed with DI water and lyophilized, before image acquisition on a Zeiss Merlin SEM (5 keV with secondary electron detection).

2.4.2. Injectability
Syringe injectability of cryogel scaffolds was assessed as reported previously [19], and adapted to reflect the *in vivo* injection procedure. Briefly, 3D printed cryogel scaffolds were dehydrated by compression with sterile gauze. They were then inserted into a syringe and delivered into excess water or cell culture medium through a catheter with an inner diameter of 0.8 mm (BD Biosciences). The injection was considered successful if the structures remained visually intact.

2.4.3. Pore size distribution
For pore size analysis, cryogels were cut into thin slices while still frozen. The slices were then thawed, imaged in bright field (10× objective) and binarized. The dimensions of about 200 pores were recorded using ImageJ software for small pore (−80 °C bed temperature) and large pore (−20 °C bed temperature) areas.

2.5. Scaffold coating and cell culture

2.5.1. Collagen coating
To allow cell adhesion to the printed and autoclaved scaffolds, we coated the cryogels with collagen I. For this, the samples were dehydrated by compression against sterile gauze. They were then immersed into sterile DI water, followed by MES buffer (pH = 4.5, 250 mM), followed by collagen coating solution for 5 min, with dehydration against the gauze for each step. The collagen coating solution contained 0.3 mg/mL collagen I diluted in MES buffer pH 4.5, 100 mM. After the coating step, scaffolds were rinsed two times with sterile DI water. Crosslinking of the collagen onto the CMC scaffolds was performed by immersing the previously rinsed scaffolds into a solution containing EDC (10 mg/mL in MES buffer pH 4.5, 100 mM) for 5 min. The scaffolds were further rinsed with sterile DI water and with a solution of Na_2CO_3 100 mM. Possible activated residues of EDC were inactivated using a 1% solution of aminoethanol (immersion of the scaffold during at least 5 min). Final rinsing steps were performed to readjust the pH at a physiological level: rinsing with sterile DI water and with HEPES buffer at pH 7.4, 100 mM, followed by a rinse with PBS.

2.5.2. Fluorescent labelling of collagen
For the purpose of comparison of deployment and perfusion for collagen coating, we assessed the spatial distribution of the coated collagen (electronic Supplementary information 4). For this, we labelled collagen I with rhodamine isothiocyanate, as reported previously [25].

2.5.3. Cell culture
Human foreskin fibroblasts (cell line CCD-1112SK, ATCC CRL-2429) were grown in DMEM (formulation 41965) with 10% foetal bovine serum in cell culture flasks. Cells were passaged once per week, with incubation at 37 °C and 5% CO_2. Cells were used no later than passage 20 from purchase.

2.5.4. Scaffold seeding and culture
Cells were seeded onto cryogels by dehydration of the cryogels against sterile gauze followed by rehydration with an equal volume of cell suspension [19], with a typical cell concentration of about $4*10^6$ cells/mL. After seeding, the gels were incubated for about 45–60 min, before additional excess cell culture medium was added. Subsequent incubation was at 37 °C, 5% CO_2.

2.5.5. Cell morphology and viability
Cell-laden scaffolds were fixed in 4% paraformaldehyde solution in PBS. Samples were then washed in PBS, and permeabilized with 0.3% Triton X-100, in PBS. We stained cell nuclei with DAPI (4′,6-diamidino-2-phénylindole, 300 nM) and in some instances the actin filaments with phalloidin-Atto 565 (50 nM).

Confocal images were acquired on a Zeiss LSM 700 with a 20× air objective or with a 40× oil objective. For large samples, 3D fluorescence microscopy images were collected using a light-sheet microscope (Light sheet Z.1, Carl Zeiss, Germany) with an EC Plan-Neofluar 5X/0,16 lens. Typically, 200–300 z-planes were acquired in 3 sequential modes: DAPI (excitation 405 nm, emission 420–470 nm); Alexa Fluor 555 (excitation 561 nm, emission 575–615 nm); Alexa Fluor 488/647 (excitation at 488 nm and 633 nm, emission at 505–545 nm and >660 nm). The voxel size was 2.5(XY) × 7(Z) μm. Three-dimensional images were reconstructed using IMARIS x64 7.6.5.

To analyse cell seeding efficiency as a function of local pore size, layered structures with alternating large- and small-pore layers were printed (electronic Supplementary information 5), coated, seeded, incubated, and fixed and stained at 24 h. Confocal stacks with at least 50 (and up to nearly 5000) identifiable nuclei were acquired in the relevant layers, with 5 stacks at randomly chosen locations for each layer. Cell density was quantified as the number of nuclei per unit volume. The experiment was repeated twice.

Cell survival was quantified by trypan blue exclusion staining (0.4% in HEPES-buffered salt solution HBS). For this, cell viability was estimated as the ratio of non-stained to total cell counts using bright field images (Leica DM5500, 20× objective).

2.6. In vivo analysis

2.6.1. Animals
All experimental procedures were approved by the Animal Care and Use Committee of the Canton of Vaud, Switzerland. CD1 mice (females; 12–20 weeks old; n = 10 mice) were purchased from Charles River (Bar Harbor, Maine, USA) and hosted in our facilities. All animals were kept at constant room temperature 22 ± 2 °C. They were fed a normal diet and kept under a controlled 12 h light/dark cycle.

2.6.2. Injection of scaffolds
Animals were anesthetized with 4% isoflurane USP-PPC (Animalcare Ltd) for induction, with a reduction to 1.5–2% during intervention, and protection of the eyes by application of ophthalmic liquid gel (Viscotears, Alcon). Prior to injection of samples, back hair was shaved off and the skin disinfected locally with betadine (Mundi Pharma Medical Company). Throughout the surgical procedures, sterility measures were upheld. To inject the scaffolds, the skin was gently pierced using an 18G needle. Then, a flexible catheter of 20G (BD Biosciences) was introduced subcutaneously through the orifice and the samples contained in a 2.5 mL syringe (BD Biosciences) were injected along with a small excess of PBS. To prevent leaking of fluid, the sample injection was

performed at a horizontal distance of 1 cm from the skin opening site.

Two scaffold samples were separately and independently implanted into each mouse. All animals were monitored for the following 3 months by animal care services.

2.6.3. Sacrifice and samples harvesting

Mice were sacrificed 12 weeks after the injection procedure. For this mice were anesthetized with sodium pentobarbital (150 mg/kg, I.P) and transcardially perfused with PBS supplemented with 4% paraformaldehyde. Implants and surrounding tissues were dissected and collected. Tissue samples were post-fixed overnight in 4% paraformaldehyde at 4 °C, rinsed three times with PBS and embedded in paraffin according to standard histological procedures. Slices of 4 μm in thickness were obtained in the central area of the sample using a microtome (Leica RM2256). Selected slides were stained with haematoxylin and Eosin using an automated process (TISSUE-TEK PRISMA SPECIAL STAINER; GLAS G2 COVERSLIPPER from Sakura), enabling to assess morphology and presence of blood vessels.

2.6.4. Statistical analysis

Error bars in graphics correspond to a single sample standard deviation. Comparisons between individual conditions were performed using unpaired t-tests, with Bonferroni multiple testing correction for multiple related tests where appropriate.

3. Results

3.1. Additive manufacturing of robust cryogel scaffolds

Our goal was the 3D printing of injectable hierarchical scaffolds. A schematic overview is given in Fig. 1. We printed cryogel inks onto a freezing stage for freeform 3D structuration (Fig. 1A). Scaffolds underwent 4D shape change [21,23] for minimally invasive delivery, exhibiting rapid volume and shape recovery post-deployment (Fig. 1B). Manipulation of cryogel pore structure led to hierarchically ordered scaffolds, which could be used to direct local tissue architecture. (Fig. 1C).

We used a microextrusion approach [24,39] for cryogel printing since it is currently the most common and affordable 3D printer type [40]. First, pneumatic pressure (approx. 600 mbar) drove activated cryogel mix into the printer head (Fig. 1A). Then, liquid cryogel premix was extruded onto a freezing cold stage [41], with a modified commercial PRotos v2 3D printer (Fig. 1A). We adjusted the reaction mix [19] to reduce room temperature gelation, thereby allowing 3D-printing completion before premix could gel and clog the system (electronic Supplementary information 1, Fig. S1-1; electronic Supplementary information 2, Figs. S2-3 and S2-4 for rheological characterization). To do so, we changed the buffer system [19] to HEPES, pH 7.4, because the high pH slows the carbodiimide crosslinking chemistry (electronic Supplementary information 1, [42]). To deposit premix, we commandeered a signal intended for molten plastic extrusion to instead open an electrovalve. This modification enabled timed ejection of cryogel ink that would freeze rapidly upon stage contact, thus providing a practical method for additive, free-form manufacturing of cryogels. In comparison with previous carboxymethyl-cellulose-based cryogel formulations [19,25], this also effectively improves scaffold pore interconnectivity (electronic Supplementary information 1, Fig. S1-3).

One of the major challenges in microextrusion printing is poor adhesion between subsequently printed deposits [26]. Without sufficient layer-to-layer adhesion, 3D-printed gels will fracture when deformed. Such fragility is particularly undesirable when developing highly deformable scaffolds for injection. We solved this issue by extending the reaction time to about 30 min at room temperature (electronic Supplementary information 1, Fig. S1-1). This is not only convenient for 3D printing, but maybe more importantly ensures robust covalent crosslinking between freshly printed layers and previously printed layers underneath (Fig. S1-2). Additionally, with cryogel printing it is necessary to account for ice crystal condensation from ambient humidity on previously deposited layers. We addressed this by increasing the precursor extrusion rate to deposit a sufficient thermal mass to melt ice crystals, thereby also allowing slight local mixing enhancing layer-to-layer adhesion (Fig. S1-2).

With these optimized printing conditions, we obtained contiguous, mechanically robust cryogel scaffolds in the desired shapes.
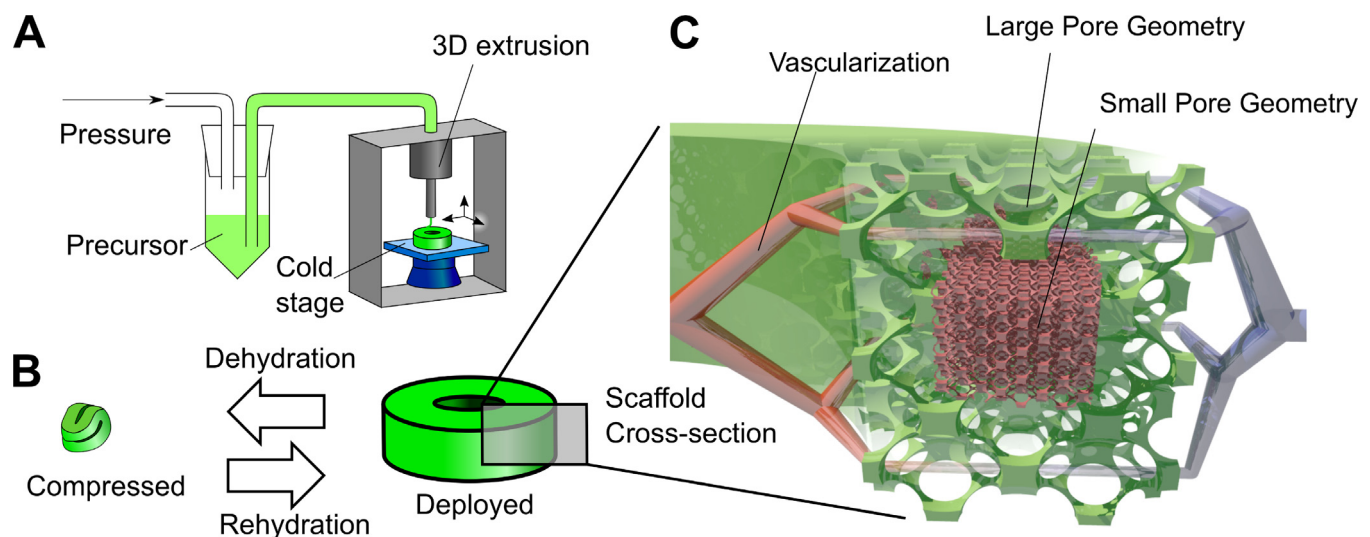

Fig. 1. Principle of 3D Cryogel Printing. A) Illustration of 3D printing of cryogels. A viscous precursor solution was printed through a modified commercial printer onto a freezing cold stage. The liquid froze upon stage contact, leading to local self-organization of ice crystals and polymer. After curing at −20 °C and thawing, we obtained a cryogel in the desired shape (in this example, a torus). B) Illustration of the 4D shape change. By withdrawing fluid, the cryogel was highly dehydrated and compressed; in addition, surface tension drove surface-minimizing folding. Upon rehydration, the cryogel returned to its original shape and volume via shape memory. The switch between compressed and deployed cryogel state was reversible, could be repeated many times, and was used for minimally invasive delivery. C) Illustration of the hierarchical scaffold organization. Local pore size variation was used to preferentially drive *in vitro* cellular organization and *in vivo* vascularization to areas with large pores.

Mechanical characterization indeed indicates a Young modulus on the order of 1kPa and repeated reversible compressibility (electronic Supplementary information 3). For convenience of sample transport, we did not print directly onto the cooled printer stage, but rather onto a polypropylene sheet (0.5 mm) reversibly attached to the stage with a drop of isopropanol.

3.2. 3D scaffold injection through 4D compressional deployment

We then investigated the 4D compressional shape change [21,23] of a range of 3D-printed structures (Fig. 2). For visualization, we stained scaffolds with methylene blue. To test injection capacity, structures were first partially dehydrated by capillary withdrawal of fluid (Fig. 2A and B, "Dehydrated"). Using tweezers, the compressed scaffolds were then transferred into the tip of a 1 mL syringe that was prefilled with excess water. A 0.8 mm catheter was mounted onto the syringe and the structures were ejected into a large water bath (Fig. 2A and B, "0s"). Once in contact with water, the collapsed structures expanded to their original shape and volume within seconds (Fig. 2A and B, "5s"). Thus, 4D deployment offers a realistic solution for the minimally invasive delivery of contiguous 3D structures.

The partial dehydration step, accompanied by extreme compression and folding, allowed for intact scaffold passage through a narrow conduit, even for structures ranging up to several cm in size. For example, we injected a porous structure with a ratio of 50 between the largest linear dimension (40 mm) and the injection cannula (0.8 mm) (Fig. 2B). Such a ratio illustrates the potential for undamaged delivery of bulky 3D-printed shapes in vivo. Further, we performed a simultaneous injection of multiple compressed shapes, which then expanded and deployed independently (Fig. 2C). Therefore, this platform could be adapted for co-delivery of several specialized structures at the same location in vivo.

3.3. Scaffold loading and minimally invasive cell delivery

Once we verified the exceptional 4D deployment capabilities, we sought to apply our 3D-printed scaffolds for cell delivery [20,29]. Cryogels typically require adhesion motives to deliver cellular cargo [19,20,29], and we have previously shown that covalent immobilization of collagen I enabled the adhesion of the mouse fibroblast cell line NOR10 to 3D printed cryogels [25]. Here, we further investigate collagen I modification of cm-scale cryogel structures. The diffusion of collagen [43] is indeed slow on a mm to cm scale, suggesting the need for pore fluid movement to efficiently and homogeneously coat the 3D printed cryogels. In the literature, both perfusion and dehydration-rehydration are proposed for cryogel fluid exchange [20,25,44]. We compared the two methods for achieving large volume coatings (electronic Supplementary information 4, Fig. S4-1) and found that dehydration-rehydration was not only easier but also provided superior collagen coating homogeneity (electronic Supplementary information 4, Figs. S4-3 and S4-4). To efficiently incorporate cells, we partially dehydrated collagen coated scaffolds and rehydrated with a cellular suspension [19,20,25] of human foreskin fibroblasts. Thus, the 4D dehydration-rehydration cycle allowed for both rapid coating and rapid cell seeding of 3D cryogel scaffolds.

After the establishment of a loading protocol, we 3D-printed, coated, and seeded star shaped structure (Fig. 3). We analysed cellular distribution via confocal microscopy and observed cell seeding throughout the entire scaffold, with slightly higher cell density near the surfaces (Fig. 3A). Magnification of the scaffold reveals the attainment of high local cell densities in our cryogels (Fig. 3B). Finally, we validated the minimally invasive delivery of seeded cryogel structures. We stained cells to examine cellular viability before and after dehydration, injection through 0.8 mm cannula (compression ratio of 6.25 between maximal linear dimension of the structures and cannula inner diameter), and subsequent rehydration (Fig. 3C). We found no significant difference between injected and non-injected samples regarding viability and total cell number (P = 0.08 respectively 0.06). This indicates that cellular viability is approximately maintained despite the extensive folding and compression that occurs during 4D scaffold deployment. Detailed investigation of cell viability in electronic Supplementary information 6 indicates that cell protection is guaranteed by pore fluid evacuation rather than cell compression for as long as open pore space is available (Figs. S6-1, S6-2). As such, injectable 3D-printed cryogels offer a promising platform for minimally invasive delivery of cell-laden scaffolds.
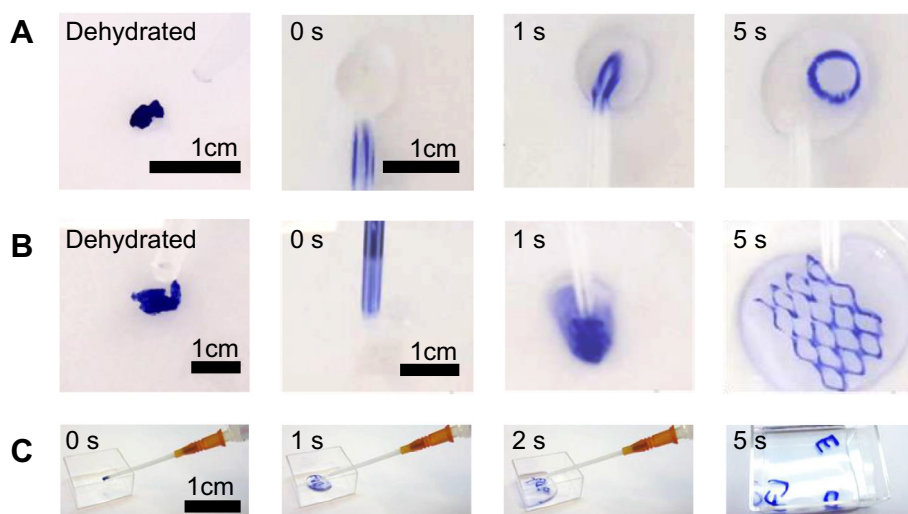

Fig. 2. 4D deployment procedure of 3D-printed scaffolds. A) The 4D deployment procedure. This shows the dehydration-based compression, injection sequence, and scaffold expansion of a 3D-printed circular structure. B) 4D deployment of a large porous scaffold. By printing cm-scale pores, very large structures can be ejected without damage (here, a 3 × 4 cm structure through a 0.8 mm catheter). C) Simultaneous deployment of individual structures. A set of letters was printed and stained with methylene blue. The sequence shows ejection through a catheter and subsequent expansion to original size and shape in water. Video files are available as electronic Supplementary material.
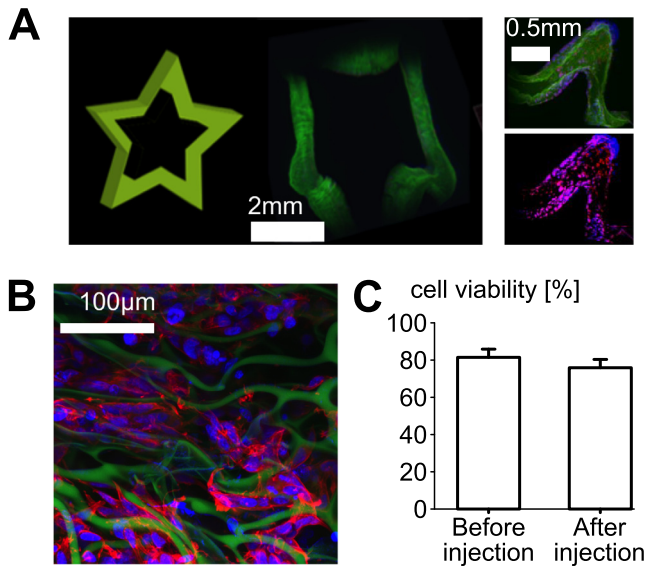
Fig. 3. Confocal microscopy of 3D-printed, cell-seeded structure. A) Scheme and Light sheet microscopy images of a star shaped structure seeded with human foreskin fibroblasts. Upper insert with all fluorescence channels, lower insert showing cells only. Nuclei were labelled with DAPI (blue), actin cytoskeleton labelled with phalloidin (red), gel labelled with aminofluorescein (green). Intensity of the blue and red channel was increased proportionally in the lower inset for better visibility of these two channels. B) Close-up of the cell-seeded structure. Confocal imaging illustrated the local cell densities attained within 3D-printed cryogel scaffolds, staining as in Fig. 3A. C) Viability measurement before and after injection. We stained seeded cells with Trypan blue to examine the viability before and after a scaffold injection sequence. All scaffolds used in this figure were produced by printing at −20 °C. (For interpretation of the references to colour in this figure legend, the reader is referred to the web version of this article.)

3.4. Design of hierarchically ordered scaffolds to control cellular densities

We developed a method to fabricate freeform cryogel structures (Fig. 1), capable of enduring extreme 4D deployment cycles (Fig. 2) for minimally invasive cell delivery (Fig. 3). After achieving these goals, we investigated the possibility of constructing hierarchically ordered scaffolds. We have previously shown that by variation of the 3D printing process temperatures, it is possible to modulate the local pore size in the printed product [25]. We have shown that this allows modulation of cell seeding density *in vitro* [25]. Here, we address whether variable pore size structure can be used *in vivo* to direct tissue ingrowth and scaffold vascularization.

A mean pore diameter of 50 μm was reported to be critical threshold for vascularization of porous scaffolds [27,28]. To test whether pore size could be used to direct vascularization, we therefore needed to identify a set of conditions for the attainment of substantially smaller mean pore size and substantially larger mean pore size in distinct large pore (LP) and small pore (SP) regions.

To achieve the desired pore size ranges substantially below and above the threshold of 50 μm, we exploit the known dependency of pore size on heat transfer during printing [18,25]. To produce small pore (SP) cryogels, the heat transfer rate should be maximal [18], so we used dry ice to cool the printing substrate to −80 °C. This is known to lead to pore sizes in the 20 μm range [25]. For large pores (LP), we employed a higher substrate temperature of −20 °C, maintained by more distal, pre-determined placement of the dry ice. By itself, this substrate temperature difference is not sufficient to achieve the desired pore size contrast [25], so we proceeded with further optimizations. We added a polypropylene layer (0.5 mm height) to reduce heat conduction and optimized the printing parameters to achieve the desired large pore size range while maintaining adequate printing quality and resolution (electronic Supplementary information 2).

With the optimized conditions, we obtain sharp transitions from SP areas to LP areas (Fig. 4A). To validate that the observed boundary truly coincides with temperature change, we changed from red-labelled to green-labelled ink when changing substrate temperature (SP to LP). Our results confirmed that the pore size transition sharply localizes to the boundary between the two labelled inks (Fig. 4B).

We quantified the pore size distribution obtained at −80 °C (SP) and −20 °C (LP) and found almost an order of magnitude difference in mean pore size, with 16 ± 4 μm for SP and 127 ± 42 μm for LP (Fig. 4C). Notably, these values bracket the critical threshold of
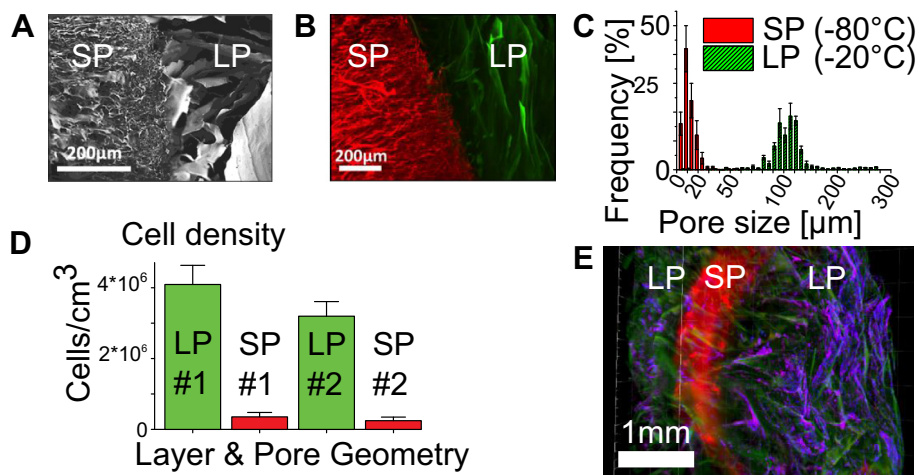

Fig. 4. Control over local pore size and cell seeding density. A) Scanning electron micrograph of the boundary between a small pore (SP) region, deposited at −80 °C, and a large pore region (LP), deposited at −20 °C. B) Confocal micrograph of a similar boundary region. The small pore (SP) region was printed with red fluorescent labelling, and the large pore (LP) region with green labelling. C) Quantification of the pore size distribution in the SP and LP areas. D) Quantitative analysis of the influence of pore size on cell seeding. Heterogeneous scaffolds with a layer sequence of large pore (LP) – small pore (SP) – LP – SP were used. Scaffolds were coated with collagen, seeded with human foreskin fibroblasts, and fixed after 24 h of culture and stained. The local cell density was determined from confocal images, as the number of DAPI-stained nuclei per unit volume. E) Volume viewer image of a confocal stack of a mixed-methods cryogel scaffold, featuring a 3D-printed SP torus (red) embedded within a moulded LP block (green). Cells were stained for nuclei (DAPI, blue) and actin (phalloidin, red). (For interpretation of the references to colour in this figure legend, the reader is referred to the web version of this article.)

50 µm required for vascularization [27,28]. It has been reported that when seeding heterogenous porous scaffolds with pore sizes larger and smaller than the cell size, cell seeding was limited to the large pore size area due to steric exclusion effects [25]. Here, we sought to assess whether the local scaffold geometry could be used to control cell seeding densities *in vitro* also when both large and small pores exceed the diameter of the isolated cells in suspension. To do so, we fabricated stratified structures with alternating LP and SP layers (electronic Supplementary information 5, Fig. S5-1). We coated and seeded scaffolds by dehydration-rehydration and quantified volumetric cell density 24 h post-seeding. In the first LP layer, cell density is nearly equal to the original seeding density (4×10^6 cells/mL) whereas the first SP layer efficiently excludes cells (Fig. 4D). Further, cell density in the second LP layer was also relatively high despite the barrier of the first SP layer, even though the cell suspension can only access this layer LP laterally. Our hypothesis is that due to the lower fluidic resistance of the LP layers, fluid and cells will preferentially first follow the LP areas during seeding, leading to deep seeding of LP layers, whereas nearly cell-free fluid later hydrates the SP areas.

After validating the effect of local geometry on cell seeding, we investigated the combination of different additive manufacturing techniques. Printing is appropriate for intricate structures but is highly inefficient for large, basic shapes. Therefore, we were specifically interested in sequential fabrication using 3D cryogel printing and 3D cryogel molding. We started by 3D-printing a SP torus. Then, we used moulding to rapidly cast a large LP block around the torus. Thus, we efficiently obtained a complex scaffold featuring a precise SP torus shape embedded within a simple LP block shape. Cell staining after seeding revealed a low density of cells within the 3D-printed SP torus, contrasting with the high density of cells within the moulded LP block (Fig. 4E). This shows that blending different 3D manufacturing methods allows rapid assembly of locally heterogeneous cryogel scaffolds, while conserving the ability to direct cellular densities *in vitro*.

3.5. Biocompatibility and influence of hierarchical scaffolds on tissue architecture

After demonstrating the effect of hierarchically designed scaffolds on cellular densities *in vitro*, we wanted to assess the *in vivo* behaviour of our 3D-printed cryogel scaffolds. First, we needed to assess basic biocompatibility, ensuring absence of encapsulation. Second, we sought to determine the effect of local pore geometry on the tissue architecture, particularly regarding scaffold infiltration and vascularization densities. We 3D-printed and implanted three different scaffolds: homogenous large pore, homogenous small pore, and heterogeneous scaffold with large and small pores (for pore size quantification, see Fig. 4C), organized in parallel stripes of 1 mm diameter and a total area of 1 cm × 1 cm. We injected the scaffolds into the subcutaneous space in mice via the 4D deployment effect. Sterile scaffolds were dehydrated by the capillary action of sterile gauze, loaded into 1 mL syringes, and injected using 0.8 mm soft catheters after a small incision in the skin. The scaffolds deployed *in vivo*, due to the uptake of a small excess of PBS co-injected with the scaffolds. Scaffold shape and volume remained stable based upon visual inspection of externally visible scaffold bumps in mice (Fig. 5A).

Three months post-implantation, the scaffolds exhibited good biocompatibility without any particular signs of encapsulation. Scaffolds were infiltrated with a non-specific loose fibrous tissue [45,46] with minimal signs of inflammation (Fig. 5B). However, infiltration density and organization varied substantially with the local scaffold geometry (Fig. 5B). In LP areas the tissue was seen as contiguous. Cells with elongated nuclei and light cytoplasm, presumably fibroblasts, were frequent and intermingled with loose fibbers. In SP areas some clear-staining fibroblasts were observed, but colonization was restricted to a sporadic arrangement with less contiguous fibrillary material and more dark-staining immune cells. Blood vessels were frequent in LP areas but were quite rare in the SP areas. These *in vivo* tissue integration results were confirmed by further staining for tissue morphology, and collagen and blood vessel presence (electronic Supplementary information 7, Fig. S7-1). To better characterize the influence of local pore size on tissue architecture, we quantified the number of visible blood vessels (labelled with stars, Fig. 5B) per unit area. As expected, we found a much smaller blood vessel density for small pore areas versus large pore areas (Fig. 5C). This difference was observed between homogenous SP and homogenous LP scaffolds, and between individual SP and LP sections of the heterogeneous scaffolds. The results provide a proof-of-principle that local cryogel
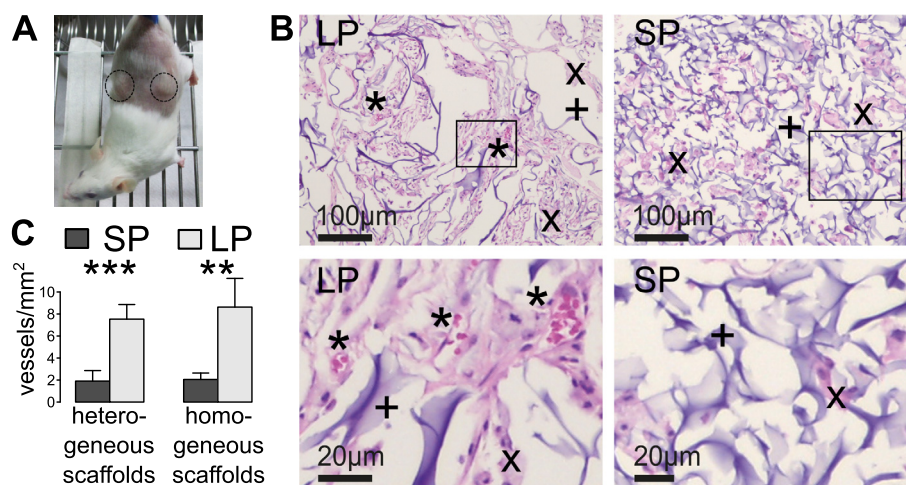

Fig. 5. *In vivo* assessment of 3D printed scaffolds. A) Visual scaffold appearance after minimally invasive implantation into the subcutaneous space (dorsal location), 3 months after the injection. B) Histological sections (Haematoxylin/Eosin staining) at 3 months, of large pore areas (LP) and small pore areas (SP) at both low and high magnification. Asterisks (*) designate examples of visible blood vessels (identified by pink red blood cells), plus signs (+) indicate sample scaffold pieces (dark purple), whereas x designates sample areas of cellular invasion. C) Quantification of blood vessels identifiable on 20× images by the presence of red blood cells per unit area. We performed the quantification in heterogeneous scaffolds (possessing both large pore and small pore areas), and in separate homogeneous scaffolds (possessing either only large pores or only small pores). (For interpretation of the references to colour in this figure legend, the reader is referred to the web version of this article.)

variation can be used to direct preferential tissue evolution in larger 3D-printed scaffolds.

4. Discussion

We here demonstrated 3D-printing and 4D deployment of cryogel scaffolds for efficient coating, seeding, and minimally invasive cell delivery. Further, we manipulated local scaffold geometry to control *in vitro* cell seeding densities and *in vivo* tissue architecture.

3D printing offered free-form fabrication, rapid prototyping and control over scaffold properties [25,47–49]. Cryogel technology provided 4D deployment for minimally invasive delivery, facile coating and seeding, cellular protection during scaffold compression, as well as a local intricate pore structure with a spatial resolution beyond anything achievable in typical microextrusion 3D printing [19,20,25,29,41].

By combining and optimizing 3D printing and cryogelation, we generated soft free-form scaffolds with shape memory that could robustly endure 4D dehydration-rehydration deployment sequences for minimally invasive delivery. The 3D printed organization allowed us to further enhance compressibility and increase the size of structures amenable to minimally invasive delivery. For example, we demonstrated a rhomboid network where the largest linear dimension of the structure was 50x greater than the application catheter (Fig. 2), compared to the previous maximum dimension ratio of 20 that we achieved with non-structured cryogels [19].

Compared to recent advances in 4D hydrogel printing [23], cryogel technology allows for 3D-printing of the final desired gel structure in the equilibrium shape. This advantage eliminates the need to mathematically solve the inverse problem of folding [23], and greatly simplifies printing by eliminating the requirement for fibre alignment [23]. Further, our combination of 4D deployment and local pore size control enabled fine local control over cell seeding density *in vitro*. Here, we controlled substrate temperature by manually displacing dry ice, which is a basic and slow process necessitating user intervention. However, it is fully possible to automate and accelerate temperature switching during cryogenic printing, for instance by combining a heating resistance with dry ice cooling [25].

In vivo, spontaneous colonization and vascularization has been observed for porous scaffolds in the subcutaneous space [27,28], although growth factor delivery was sometimes required for vascularization [36]. We observed ingrowth of loosely fibrillar vascularized tissue [27,28] in cell-free 3D-printed cryogel scaffolds without any need for growth factors and without any signs of encapsulation. Vascularization was strongly influenced by pore geometry [27,28], and we found that local pore structure determined vascularization independently of the composition of the remainder of the scaffold. Large pore areas in a scaffold always display high vascularization density, even if there are also small pore areas within the same scaffold. Conversely, vascularization density is always low in small pore areas, even if surrounding large pore areas facilitate access [45] for tissue infiltration. This precise variation of local properties of 3D-printed scaffolds can be considered the 5th dimension of bioprinting [22]. By controlling this local printing dimension, we developed sophisticated 3D shapes that exhibit different effects at different locations within the same continuous structure. For example, we could use this to direct vascularization architecture to regulate local oxygen tensions for stem cell niches [50].

In addition to unique pore structures, we showed the feasibility of printing with multiple different inks. Cryogels can be formed from many different monomers with many different crosslinking chemistries [18]. By adapting reaction rates, most hydrogels could feasibly be used in the 3D cryogel printing technology we developed here. This provides a minimally invasive platform that can be modified not just for desired 3D shape and local pore size, but also for customized cell adhesion [20], differentiation [51], stiffness [19], biodegradation [52], and growth factor delivery [29]. Lastly, cryogels are valuable tools for minimally invasive cell transplantation [20,29]. We showed that cell viability can be preserved during 4D compression and redeployment of 3D-printed cryogels. Our next goal is to transplant cell-seeded 3D-printed structures *in vivo* to drive specific tissue generation [53].

5. Conclusions

We developed a novel platform to address the unmet need of freeform fabrication of injectable, hierarchical scaffolds for tissue engineering. We employed 3D printing to manufacture robust cryogels that could endure extreme dehydration-rehydration compression cycles. Then, we illustrated the usefulness of this property for minimally invasive cell delivery. Lastly, we manipulated the cryogelation process to obtain hierarchically ordered scaffolds. By precisely directing local scaffold geometry within a greater 3D structure, we demonstrated fine control over cell seeding densities *in vitro*, as well as tissue infiltration and scaffold vascularization *in vivo*.

6. Declaration of competing interests

AB, PR and TB declare having financial interests in the company Volumina-Medical SA. The other authors declare no competing interests.

Appendix A. Supplementary data

Supplementary data associated with this article can be found, in the online version, at https://doi.org/10.1016/j.actbio.2018.05.056.

References

[1] P. Bajaj, R.M. Schweller, A. Khademhosseini, J.L. West, R. Bashir, 3D biofabrication strategies for tissue engineering and regenerative medicine, Annu. Rev. Biomed. Eng. 16 (2014) 247–276.

[2] V. Lee, G. Singh, J.P. Trasatti, C. Bjornsson, X. Xu, T.N. Tran, S.S. Yoo, G. Dai, P. Karande, Design and fabrication of human skin by three-dimensional bioprinting, Tissue Eng. Part C Methods 20 (6) (2014) 473–484.

[3] W. Lee, J. Pinckney, V. Lee, J.H. Lee, K. Fischer, S. Polio, J.K. Park, S.S. Yoo, Three-dimensional bioprinting of rat embryonic neural cells, Neuroreport 20 (8) (2009) 798–803.

[4] B.C. Wengerter, G. Emre, J.Y. Park, J. Geibel, Three-dimensional printing in the Intestine, Clin. Gastroenterol. Hepatol. 14 (8) (2016) 1081–1085.

[5] A. Faulkner-Jones, C. Fyfe, D.J. Cornelissen, J. Gardner, J. King, A. Courtney, W. Shu, Bioprinting of human pluripotent stem cells and their directed differentiation into hepatocyte-like cells for the generation of mini-livers in 3D, Biofabrication 7 (4) (2015) 044102.

[6] M.M. Laronda, A.L. Rutz, S. Xiao, K.A. Whelan, F.E. Duncan, E.W. Roth, T.K. Woodruff, R.N. Shah, A bioprosthetic ovary created using 3D printed microporous scaffolds restores ovarian function in sterilized mice, Nat. Commun. 8 (2017) 15261.

[7] A.A. Fretland, A. Sokolov, N. Postriganova, A.M. Kazaryan, S.E. Pischke, P.H. Nilsson, I.N. Rognes, B.A. Bjornbeth, M.W. Fagerland, T.E. Mollnes, B. Edwin, Inflammatory response after laparoscopic versus open resection of colorectal liver metastases: data from the Oslo-CoMet Trial, Medicine (Baltimore) 94 (42) (2015) e1786.

[8] G. Gandaglia, K.R. Ghani, A. Sood, J.R. Meyers, J.D. Sammon, M. Schmid, B. Varda, A. Briganti, F. Montorsi, M. Sun, M. Menon, A.S. Kibel, Q.D. Trinh, Effect of minimally invasive surgery on the risk for surgical site infections: results from the National Surgical Quality Improvement Program (NSQIP) Database, JAMASurg 149 (10) (2014) 1039–1044.

[9] E. Schippers, A. Tittel, A. Ottinger, V. Schumpelick, Laparoscopy versus laparotomy: comparison of adhesion-formation after bowel resection in a canine model, Dig. Surg. 15 (2) (1998) 145–147.

[10] S.G. Levrant, E.J. Bieber, R.B. Barnes, Anterior abdominal wall adhesions after laparotomy or laparoscopy, J. Am. Assoc. Gynecol. Laparosc. 4 (3) (1997) 353–356.

[11] E. Shariati, J. Bakhtiari, A. Khalaj, A. Niasari-Naslaji, Comparison between two portal laparoscopy and open surgery for ovariectomy in dogs, Vet. Res. Forum. 5 (3) (2014) 219–223.

[12] J.G. Hardy, M. Palma, S.J. Wind, M.J. Biggs, Responsive biomaterials: advances in materials based on shape-memory polymers, Adv. Mater. 28 (27) (2016) 5717–5724.

[13] M. Montgomery, S. Ahadian, L. Davenport Huyer, M. Lo Rito, R.A. Civitarese, R. D. Vanderlaan, J. Wu, L.A. Reis, A. Momen, S. Akbari, A. Pahnke, R.K. Li, C.A. Caldarone, M. Radisic, Flexible shape-memory scaffold for minimally invasive delivery of functional tissues, Nat. Mater. (2017).

[14] Y. Deng, J. Ren, G. Chen, G. Li, X. Wu, G. Wang, G. Gu, J. Li, Injectable in situ cross-linking chitosan-hyaluronic acid based hydrogels for abdominal tissue regeneration, Sci. Rep. 7 (1) (2017) 2699.

[15] S.H. Bentkover, The biology of facial fillers, Facial Plast. Surg. 25 (2) (2009) 73–85.

[16] W.O. Bank, C.W. Kerber, Gelfoam embolization: a simplified technique, AJR Am. J. Roentgenol. 132 (2) (1979) 299–301.

[17] T. Kohnen, M. Baumeister, D. Kook, O.K. Klaproth, C. Ohrloff, Cataract surgery with implantation of an artificial lens, Dtsch. Arztebl. Int. 106 (43) (2009) 695–702.

[18] O. Okay, F. Auriemma, A.D. Bannerman, C. De Rosa, R. Di Girolamo, V.I. Lozinsky, H. Mak, B. Mattiasson, P.D. Petrov, O.A. Shlyakhtin, C.B. Tsvetanov, W. Wan, L. Yang, Polymeric Cryogels: Macroporous Gels with Remarkable Properties, Springer, Cham Heidelberg New York Dordrecht London, 2014.

[19] A. Beduer, T. Braschler, O. Peric, G.E. Fantner, S. Mosser, P.C. Fraering, S. Bencherif, D.J. Mooney, P. Renaud, A compressible scaffold for minimally invasive delivery of large intact neuronal networks, Adv. Healthc. Mater. 4 (2) (2015) 301–312.

[20] S.A. Bencherif, R.W. Sands, D. Bhatta, P. Arany, C.S. Verbeke, D.A. Edwards, D.J. Mooney, Injectable preformed scaffolds with shape-memory properties, P. Natl. Acad. Sci. USA 109 (48) (2012) 19590–19595.

[21] Y. Zhou, W.M. Huang, S.F. Kang, X.L. Wu, H.B. Lu, J. Fu, H. Cui, From 3D to 4D printing: approaches and typical applications, J. Mech. Sci. Technol. 29 (10) (2015) 4281–4288.

[22] E.A. Gillaspie, J.S. Matsumoto, N.E. Morris, R.J. Downey, K.R. Shen, M.S. Allen, S. H. Blackmon, From 3-dimensional printing to 5-dimensional printing: enhancing thoracic surgical planning and resection of complex tumors, Ann. Thorac. Surg. 101 (5) (2016) 1958–1962.

[23] A.S. Gladman, E.A. Matsumoto, R.G. Nuzzo, L. Mahadevan, J.A. Lewis, Biomimetic 4D printing, Nat. Mater. 15 (2016) 413–419.

[24] Y.C. Li, Y.S. Zhang, A. Akpek, S.R. Shin, A. Khademhosseini, 4D bioprinting: the next-generation technology for biofabrication enabled by stimuli-responsive materials, Biofabrication 9 (1) (2016) 012001.

[25] L. Serex, T. Braschler, A. Filippova, A. Rochat, A. Béduer, A. Bertsch, P. Renaud, Pore size manipulation in 3D printed cryogels enables selective cell seeding, Adv. Mater. Technol. 3 (4) (2018).

[26] C. Bell, Maintaining and Troubleshooting Your 3D Printer, Springer/Apress Media, New York, 2014.

[27] Y.C. Chiu, M.H. Cheng, H. Engel, S.W. Kao, J.C. Larson, S. Gupta, E.M. Brey, The role of pore size on vascularization and tissue remodeling in PEG hydrogels, Biomaterials 32 (26) (2011) 6045–6051.

[28] A. Artel, H. Mehdizadeh, Y.C. Chiu, E.M. Brey, A. Cinar, An agent-based model for the investigation of neovascularization within porous scaffolds, Tissue Eng. Part A 17 (17–18) (2011) 2133–2141.

[29] S.A. Bencherif, R. Warren Sands, O.A. Ali, W.A. Li, S.A. Lewin, T.M. Braschler, T.Y. Shih, C.S. Verbeke, D. Bhatta, G. Dranoff, D.J. Mooney, Injectable cryogel-based whole-cell cancer vaccines, Nat. Commun. 6 (2015) 7556.

[30] U. Zimmermann, G. Klock, K. Federlin, K. Hannig, M. Kowalski, R.G. Bretzel, A. Horcher, H. Entenmann, U. Sieber, T. Zekorn, Production of mitogen-contamination free alginates with variable ratios of mannuronic acid to guluronic acid by free flow electrophoresis, Electrophoresis 13 (5) (1992) 269–274.

[31] H. Seyednejad, D. Gawlitta, R.V. Kuiper, A. de Bruin, C.F. van Nostrum, T. Vermonden, W.J. Dhert, W.E. Hennink, In vivo biocompatibility and biodegradation of 3D-printed porous scaffolds based on a hydroxyl-functionalized poly(epsilon-caprolactone), Biomaterials 33 (17) (2012) 4309–4318.

[32] D.J. Modulevsky, C.M. Cuerrier, A.E. Pelling, Biocompatibility of subcutaneously implanted plant-derived cellulose biomaterials, PLoS One 11 (6) (2016) e0157894.

[33] S.T. Koshy, T.C. Ferrante, S.A. Lewin, D.J. Mooney, Injectable, porous, and cell-responsive gelatin cryogels, Biomaterials 35 (8) (2014) 2477–2487.

[34] M. Leonardis, A. Palange, New-generation filler based on cross-linked carboxymethylcellulose: study of 350 patients with 3-year follow-up, Clin. Interv. Aging 10 (2015) 147–155.

[35] K.Y. Lee, E. Alsberg, D.J. Mooney, Degradable and injectable poly(aldehyde guluronate) hydrogels for bone tissue engineering, J. Biomed. Mater. Res. 56 (2) (2001) 228–233.

[36] M. Yamamoto, Y. Tabata, H. Kawasaki, Y. Ikada, Promotion of fibrovascular tissue ingrowth into porous sponges by basic fibroblast growth factor, J. Mater. Sci. – Mater. Med. 11 (4) (2000) 213–218.

[37] B.S. Shah, M. Chen, T. Suzuki, M. Embree, K. Kong, C.H. Lee, L. He, L. Xiang, J.A. Ahn, S. Ding, J.J. Mao, Pyrintegrin induces soft tissue formation by transplanted or endogenous cells, Sci. Rep. 7 (2017) 36402.

[38] L. De Laporte, L.D. Shea, Matrices and scaffolds for DNA delivery in tissue engineering, Adv. Drug Deliv. Rev. 59 (4–5) (2007) 292–307.

[39] S. Knowlton, S. Onal, C.H. Yu, J.J. Zhao, S. Tasoglu, Bioprinting for cancer research, Trends Biotechnol. 33 (9) (2015) 504–513.

[40] S.V. Murphy, A. Atala, 3D bioprinting of tissues and organs, Nat. Biotech. 32 (8) (2014) 773–785.

[41] C. Wang, Q. Zhao, M. Wang, Cryogenic 3D printing for producing hierarchical porous and rhBMP-2-loaded Ca-P/PLLA nanocomposite scaffolds for bone tissue engineering, Biofabrication 9 (025031) (2017).

[42] A. Williams, I.T. Ibrahim, A new mechanism involving cyclic tautomers for the reaction with nucleophiles of the water-soluble peptide coupling reagent 1-ethyl-3-(3'-(dimethylamino)propyl)carbodiimide (EDC), J. Am. Chem. Soc. 103 (24) (1981) 7090–7095.

[43] F.H. Silver, K.H. Langley, R.L. Trelstad, Type I collagen fibrillogenesis: initiation via reversible linear and lateral growth steps, Biopolymers 18 (10) (1979) 2523–2535.

[44] E. Jain, A. Kumar, Disposable polymeric cryogel bioreactor matrix for therapeutic protein production, Nat. Protoc. 8 (5) (2013) 821–835.

[45] M.C. Wake, A.G. Mikos, G. Sarakinos, J.P. Vacanti, R. Langer, Dynamics of fibrovascular tissue ingrowth in hydrogel foams, Cell Transplant. 4 (3) (1995) 275–279.

[46] I. Dal Pra, G. Freddi, J. Minic, A. Chiarini, U. Armato, De novo engineering of reticular connective tissue in vivo by silk fibroin nonwoven materials, Biomaterials 26 (14) (2005) 1987–1999.

[47] A. Munaz, R.K. Vadivelu, J. St, M. John, H. Barton, N.-T. Nguyen Kamble, Three-dimensional printing of biological matters, J. Sci.: Adv. Mater. Devices 1 (1) (2016) 1–17.

[48] T.J. Hinton, Q. Jallerat, R.N. Palchesko, J.H. Park, M.S. Grodzicki, H.J. Shue, M.H. Ramadan, A.R. Hudson, A.W. Feinberg, Three-dimensional printing of complex biological structures by freeform reversible embedding of suspended hydrogels, Sci. Adv. 1 (9) (2015) e1500758.

[49] M. Heller, H.K. Bauer, E. Goetze, M. Gielisch, K.E. Roth, P. Drees, G.S. Maier, B. Dorweiler, A. Ghazy, M. Neufurth, W.E. Muller, H.C. Schroder, X. Wang, C.F. Vahl, B. Al-Nawas, Applications of patient-specific 3D printing in medicine, Int. J. Comput. Dent. 19 (4) (2016) 323–339.

[50] H. Abdollahi, L.J. Harris, P. Zhang, S. McIlhenny, V. Srinivas, T. Tulenko, P.J. DiMuzio, The role of hypoxia in stem cell differentiation and therapeutics, J. Surg. Res. 165 (1) (2011) 112–117.

[51] M. Jurga, M.B. Dainiak, A. Sarnowska, A. Jablonska, A. Tripathi, F.M. Plieva, I.N. Savina, L. Strojek, H. Jungvid, A. Kumar, B. Lukomska, K. Domanska-Janik, N. Forraz, C.P. McGuckin, The performance of laminin-containing cryogel scaffolds in neural tissue regeneration, Biomaterials 32 (13) (2011) 3423–3434.

[52] A.K. Shakya, R. Holmdahl, K.S. Nandakumar, A. Kumar, Polymeric cryogels are biocompatible, and their biodegradation is independent of oxidative radicals, J. Biomed. Mater. Res. A 102 (10) (2014) 3409–3418.

[53] D.J. Mooney, S. Park, P.M. Kaufmann, K. Sano, K. McNamara, J.P. Vacanti, R. Langer, Biodegradable sponges for hepatocyte transplantation, J. Biomed. Mater. Res. 29 (8) (1995) 959–965.